

Cooperative effects of Coulomb and electron-phonon interactions in the two-dimensional 16-band d - p model for iron-based superconductors

Yuki Yanagi,¹ Youichi Yamakawa,¹ Naoko Adachi,¹ and Yoshiaki Ōno¹

¹*Department of Physics, Niigata University, Ikarashi, Niigata 950-2181, Japan*

(Dated: February 23, 2024)

We study the electronic states and the superconductivity in the two-dimensional 16-band d - p model coupled with A_{1g} , B_{1g} and E_g local phonons and obtain the rich phase diagram including the magnetic, charge and orbital ordered phases on the parameter plane of the Coulomb and electron-phonon interactions. When the electron-phonon interaction is dominant, the charge fluctuations induce the s_{++} -wave superconductivity, while when the Coulomb interaction is dominant, the magnetic fluctuations induce the s_{\pm} -wave superconductivity. Remarkably, the orbital fluctuations are enhanced due to the cooperative effects of the Coulomb and electron-phonon interactions and induce the s_{++} -wave and the nodal s_{\pm} -wave superconductivities.

I. INTRODUCTION

The recently discovered iron-based superconductors^{1,2} $\text{RFePnO}_{1-x}\text{F}_x$ ($\text{R}=\text{Rare Earth}$, $\text{Pn}=\text{As, P}$) with a transition temperature T_c exceeding 50K³⁻⁷ have attracted much attention. At present, there are following four families of the iron-based superconductors: RFeAsO with ZrCuSiAs -type structure (1111 system), BaFe_2As_2 with ThCr_2Si_2 -type structure (122 system)^{8,9}, LiFeAs and NaFeAs with PbFCl -type structure (111 system)¹⁰⁻¹² and $\text{Fe}(\text{Se,Te})$ (11 system)^{13,14}. These systems have similar conducting Fe-pnictogen (-chalcogen) planes and the resulting electronic structures predicted by the first principle calculations are similar to those for each families¹⁵⁻²³. The energy bands near the Fermi level mainly constructed by the Fe-3d orbitals are heavily entangled and there are two or three concentric hole Fermi surfaces (FSs) around the Γ -point [$\mathbf{k} = (0,0)$] and the elliptical electron FSs around the M -point [$\mathbf{k} = (\pi,\pi)$]. These features are observed by the angle resolved photoemission spectroscopy (ARPES) in several compounds²⁴⁻²⁶. Despite the similarities of the electronic structures for the four families, it seems that the details of the gap structures are different from system to system as mentioned below and the pairing state together with the mechanism of the superconductivity for the iron-based superconductors is still controversial.

As for the 1111 system, the F nondoped compound LaFeAsO exhibits the structural transition from tetragonal (P4/nmm) to orthorhombic (Cmma) phase at a transition temperature $T = 155\text{K}$ and stripe-type antiferromagnetic (AFM) order at $T = 134\text{K}$ with a magnetic moment $\sim 0.36\mu_B$ ²⁷ at low temperature. With increasing F doping, the system becomes metallic and the AFM order disappears², and then, the superconductivity emerges for $x \sim 0.1$ with $T_c \sim 26\text{K}$. Rare-earth substitution compounds exhibit superconducting transition with higher T_c ³⁻⁷. The NMR Knight shift measurements revealed that the superconductivity of the systems is the spin-singlet pairing^{28,29}. Fully-gapped superconducting states have been predicted by various experiments such as the penetration depth³⁰, the specific heat³¹, and the

impurity effect on T_c ^{29,32}. In contrast to the above mentioned experiments, the NMR relaxation rate shows the power law behavior $1/T_1 \propto T^3$ below T_c ³³, suggesting the nodal or highly anisotropic gap structure. The other NMR measurements³⁴, however, revealed $1/T_1 \propto T^6$ below T_c and there is still controversy.

The parent compound of the 122 system BaFe_2As_2 shows the structural transition from tetragonal (I4/mmm) to orthorhombic (Fmmm) phase and the stripe-type AFM order simultaneously at a transition temperature $T = 140\text{K}$ ^{9,35}, where the magnetic moment is about $0.87\mu_B$ at low temperature³⁵. Both the electron and hole doping by the substitution Co for Fe and K for Ba induce the superconductivity^{8,36}. The T^5 -dependence of $1/T_1$ ³⁷, the exponential behavior of the penetration depth³⁸ and the ARPES^{24,39,40} suggest the fully-gapped superconductivity. The chemical pressure by substituting P for As in $\text{BaFe}_2(\text{As}_{1-x}\text{P}_x)_2$ also leads to the superconductivity with T_c up to 30K ⁴¹, where the specific heat, the penetration depth, the thermal conductivity and NMR $1/T_1$ imply the nodal or highly anisotropic gap structures.^{42,43}

In 11 system, FeTe shows the another type of the AFM order with ordering vector $\mathbf{q} = (\pi,0)$ ^{44,45}, where the magnetic moment is about $2.03\mu_B$ ^{44,45}. On the other hand, FeSe does not exhibit the magnetic order but superconducting transition at $T \sim 8\text{K}$ ¹³. The thermal conductivity⁴⁶ suggests the fully-gapped superconducting state.

Theoretically, Mazin *et al.* suggested that the fully-gapped s -wave pairing whose order parameter changes its sign between the hole FSs and the electron FSs (s_{\pm} -wave pairing) is favored due to the stripe-type AFM spin fluctuations⁴⁷. According to the weak coupling approaches based on multi-orbital Hubbard models⁴⁸⁻⁵⁹, and those based on the d - p model⁶⁰⁻⁶², the s_{\pm} -wave pairing seems to be the promising candidate for the pairing state in the iron-based superconductors. It is shown that the s_{\pm} -wave pairing is realized also in the strong coupling region by the mean field study based on the t - J_1 - J_2 model⁶³ and the exact diagonalization study based on the one-dimensional two-band Hubbard model⁶⁴. The s_{\pm} -

wave state mediated by the spin fluctuations seems to be consistent with many experiments. However, the theoretical analysis of the nonmagnetic impurity effects based on the 5-band Hubbard model shows that the s_{\pm} -wave state is very fragile against nonmagnetic impurities⁶⁵. This is in contradiction to the experimental results that the superconductivity for the iron-based superconductors is robust against nonmagnetic impurities. Therefore, the fully-gapped s -wave state without sign reversing (s_{++} -wave state) is considered to be another promising candidate for the pairing state in the iron-based superconductors.

In the previous papers^{60–62,66}, we have investigated the electronic states of the Fe_2As_2 plane in iron-based superconductors on the basis of the two-dimensional 16-band d - p model which includes the Coulomb interaction on a Fe site: the intra- and inter-orbital direct terms U and U' , the Hund's coupling J and the pair-transfer J' . Using the random phase approximation (RPA), we have found that, for $U > U'$, the s_{\pm} -wave superconductivity is realized due to the spin fluctuations with $\mathbf{q} \sim (\pi, \pi)$, while for $U < U'$, the s_{++} -wave state is realized due to the orbital fluctuations with $\mathbf{q} = (0, 0)$ ⁶⁶. In addition, we suggest that the electron-phonon interaction enhances the orbital fluctuations and plays the significant role in the realization of the s_{++} -wave superconductivity in the realistic parameter region $U > U'$. In the recent Raman spectroscopy, it is shown that the electron-phonon coupling constant for A_{1g} and B_{1g} modes are larger ($\lambda_{A_{1g}}, \lambda_{B_{1g}} \sim 0.5$)⁶⁷ than those predicted by the first principle calculations ($\lambda \sim 0.21$)¹⁹. Then, it is important to investigate the effects of the electron-phonon interaction on the electronic states and the superconductivity based on the microscopic model.

Recently, Kontani and Onari have investigated the 5-band Hubbard-Holstein model which includes the Coulomb interaction and the electron-phonon interaction due to the B_{1g} and E_g phonons at the zone center by using the RPA and have shown that the E_g phonons drastically enhance the orbital fluctuations and the s_{++} -wave superconductivity is realized by the orbital fluctuations for the realistic values of the electron-phonon coupling⁶⁸. In ref. 68, they derive the electron-phonon coupling by calculating the electrostatic potential variance for Fe-3d electrons from the four surrounding As^{3-} ions due to the oscillations of the Fe atoms assuming that the spatial extensions of the Fe-3d like Wannier functions are small. The spatial extensions of the Fe-3d like Wannier orbitals in the 5-band model, however, are very large, e. g., $\langle r^2 \rangle - \langle r \rangle^2 \sim 5.37 \text{\AA}^2$ for $d_{x^2-y^2}$ orbital in LaFeAsO ,^{69–71} in contrast to their assumption. On the other hand, in the effective model which includes both the Fe 3d orbitals and the As 4p orbitals, so called d - p model, the spatial extensions of the Wannier functions are considered to be largely reduced^{69–71}. Therefore, theoretical studies on the electron-phonon interaction based on the d - p model, are highly desired.

In the present paper, we investigate the effects of the

electron-phonon interaction on the electronic states and superconductivity based on the two-dimensional 16-band d - p model, where the A_{1g} , B_{1g} and E_g phonons at the zone center are considered. Solving the linearized Eliashberg equation with the pairing interaction obtained by using the RPA, we obtain the phase diagram on the parameter plane of the Coulomb and electron-phonon interactions.

The paper is organized as follows. In Sec. II, we introduce the two-dimensional 16-band d - p model coupled with the A_{1g} , B_{1g} and E_g local phonons and explain the formulation of the RPA with the Coulomb and electron-phonon interactions in the multi-orbital system. In Sec. III, we show the numerical results of the charge-orbital susceptibility and the gap function for the various values of the Coulomb and electron-phonon interactions. The linearized Eliashberg equation is solved and we obtain the phase diagram. Finally, we summarize the paper in Sec IV.

II. MODEL AND FORMULATION

Our model Hamiltonian is the two-dimensional 16-band d - p model^{60–62,66,72} coupled with local phonons, where 3d orbitals ($d_{3z^2-r^2}$, $d_{x^2-y^2}$, d_{xy} , d_{yz} , d_{zx}) of two Fe atoms ($\text{Fe}^1=A$, $\text{Fe}^2=B$) and 4p orbitals (p_x , p_y , p_z) of two As atoms are explicitly included. It is noted that x, y axes are directed along second nearest Fe-Fe bonds. Here, we number the Fe-3d orbitals as follows: $d_{3z^2-r^2}(1)$, $d_{x^2-y^2}(2)$, $d_{xy}(3)$, $d_{yz}(4)$, $d_{zx}(5)$.

The total Hamiltonian of the d - p model is given by

$$H = H_0 + H_{\text{int}} + H_{ph} + H_{el-ph}, \quad (1)$$

where H_0 , H_{int} , H_{ph} and H_{el-ph} are the kinetic, Coulomb interaction, phonon and electron-phonon interaction parts of the Hamiltonian, respectively. The kinetic part of the Hamiltonian is given by the following tight-binding Hamiltonian,

$$\begin{aligned} H_0 = & \sum_{i,\ell,\sigma} \varepsilon_{\ell}^d d_{i\ell\sigma}^{\dagger} d_{i\ell\sigma} + \sum_{i,m,\sigma} \varepsilon_m^p p_{im\sigma}^{\dagger} p_{im\sigma} \\ & + \sum_{i,j,\ell,\ell',\sigma} t_{i,j,\ell,\ell'}^{dd} d_{i\ell\sigma}^{\dagger} d_{j\ell'\sigma} + \sum_{i,j,m,m',\sigma} t_{i,j,m,m'}^{pp} p_{im\sigma}^{\dagger} p_{jm'\sigma} \\ & + \sum_{i,j,\ell,m,\sigma} t_{i,j,\ell,m}^{dp} d_{i\ell\sigma}^{\dagger} p_{jm\sigma} + h.c., \end{aligned} \quad (2)$$

where $d_{i\ell\sigma}$ is the annihilation operator for Fe-3d electrons with spin σ in the orbital ℓ at the site i and $p_{im\sigma}$ is the annihilation operator for As-4p electrons with spin σ in the orbital m at the site i . In eq. (2), the transfer integrals $t_{i,j,\ell,\ell'}^{dd}$, $t_{i,j,m,m'}^{pp}$, $t_{i,j,\ell,m}^{dp}$ and the atomic energies ε_{ℓ}^d , ε_m^p are determined so as to fit both the energy and the weights of orbitals for each band obtained from the tight-binding approximation to those from the density functional calculation for LaFeAsO and are listed in refs. 64 and 70. The doping concentration x corresponds to

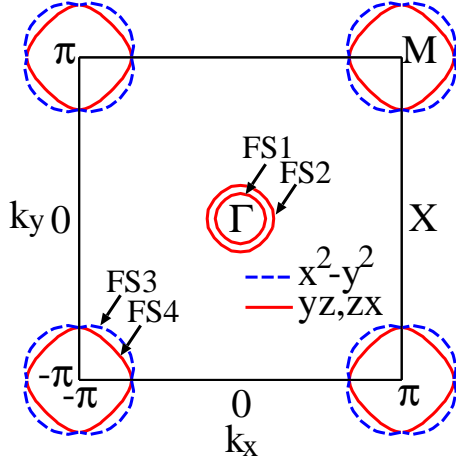


FIG. 1: (Color online) FSs obtained from the d - p model for $x = 0.1$. The solid and dashed lines show the FSs which have mainly d_{yz}, d_{zx} and $d_{x^2-y^2}$ orbital character, respectively.

the number of electrons per unit cell $n = 24 + 2x$ in the present model. The FSs for $x = 0.1$ are shown in Fig. 1 and we see the two hole FSs (FS1 and FS2) and the two electron FSs (FS3 and FS4) as predicted by the first principle calculations^{15–19}.

The Coulomb interaction part of the Hamiltonian is given as follows,

$$\begin{aligned}
 H_{\text{int}} = & \frac{1}{2}U \sum_i \sum_{\ell} \sum_{\sigma \neq \bar{\sigma}} d_{i\ell\sigma}^\dagger d_{i\bar{\ell}\bar{\sigma}}^\dagger d_{i\ell\bar{\sigma}} d_{i\bar{\ell}\sigma} \\
 & + \frac{1}{2}U' \sum_i \sum_{\ell \neq \bar{\ell}} \sum_{\sigma, \sigma'} d_{i\ell\sigma}^\dagger d_{i\bar{\ell}\sigma'}^\dagger d_{i\bar{\ell}\sigma} d_{i\ell\sigma'} \\
 & + \frac{1}{2}J \sum_i \sum_{\ell \neq \bar{\ell}} \sum_{\sigma, \sigma'} d_{i\ell\sigma}^\dagger d_{i\bar{\ell}\sigma}^\dagger d_{i\ell\sigma'} d_{i\bar{\ell}\sigma'} \\
 & + \frac{1}{2}J' \sum_i \sum_{\ell \neq \bar{\ell}} \sum_{\sigma \neq \bar{\sigma}} d_{i\ell\sigma}^\dagger d_{i\bar{\ell}\bar{\sigma}}^\dagger d_{i\bar{\ell}\sigma} d_{i\ell\bar{\sigma}}, \quad (3)
 \end{aligned}$$

where U and U' are the intra- and inter-orbital direct terms, respectively, and J and J' are the Hund's coupling and the pair-transfer, respectively. We assume that the relations between Coulomb matrix elements $U = U' + 2J$ and $J = J'$ are satisfied throughout the present paper.

Now we consider the effect of the phonon and the electron-phonon interaction parts of the Hamiltonian H_{ph} and H_{el-ph} . By performing the group theoretical analysis, it is found that there are 14 kinds of the optical phonon modes at the zone center. In the present paper, we consider the A_{1g} , B_{1g} and E_g phonon modes in which As atoms oscillate along the z -axis, Fe atoms oscillate along the z -axis and Fe atoms oscillate in the x - y plane, respectively (see Fig. 2). Here and hereafter, we neglect the momentum dependence of the electron-phonon couplings and that of the phonon frequencies for simplicity. The resulting phonon and the electron-phonon interac-

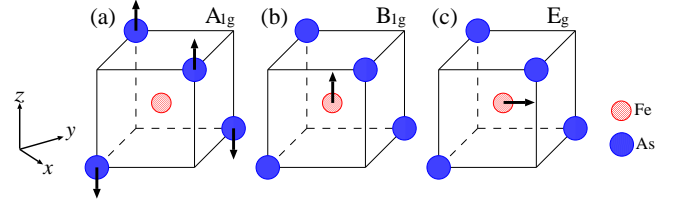


FIG. 2: (Color online) Schematic figure of the oscillations of Fe and As atoms in the (a) A_{1g} , (b) B_{1g} and, (c) E_g modes, respectively. The small and large spheres denote Fe and As atoms, respectively.

tion parts of the Hamiltonian are given as,

$$H_{ph} = \sum_i \sum_s \omega_s b_{is}^\dagger b_{is}, \quad (4)$$

$$H_{el-ph} = \sum_i \sum_s \sum_{\ell, \ell'} \sum_{\sigma} g_s^{\ell\ell'} d_{i\ell\sigma}^\dagger d_{i\ell'\sigma} (b_{is}^\dagger + b_{is}), \quad (5)$$

where b_{is} is the annihilation operator for the phonon of the mode s ($= A_{1g}, B_{1g}, E_g^1$ and E_g^2) at the site i , ω_s is the phonon frequency and $g_s^{\ell\ell'}$ is the electron-phonon coupling. We note that E_g^1 and E_g^2 correspond to the oscillation along the x - and y -axis in the E_g mode. As following ref. 68, we expand the electrostatic potential variance for Fe-3d electrons from the four surrounding As^{4-} ions due to the oscillations of the Fe atoms for the B_{1g} and E_g modes in the displacement of the Fe atoms up to the first order and expand that in the x , y and z coordinates up to the second order. The resulting electron-phonon coupling matrix elements of the B_{1g} and E_g phonons are given as follows,

$$\begin{aligned}
 \sqrt{3}g_{E_g^1}^{15} &= g_{E_g^1}^{25} = g_{E_g^1}^{34} \\
 &= -\sqrt{3}g_{E_g^2}^{14} = g_{E_g^2}^{24} = -g_{E_g^2}^{35}, \quad (6)
 \end{aligned}$$

$$g_{B_{1g}}^{44} = -g_{B_{1g}}^{55} = \sqrt{3}/2g_{B_{1g}}^{12}, \quad (7)$$

$$g_s^{\ell\ell'} = g_s^{\ell'\ell}, \quad (8)$$

$$g_s^{\ell\ell'} = 0 \quad (\text{otherwise}). \quad (9)$$

In addition, we also consider the electron-phonon coupling for the A_{1g} phonon,

$$g_{A_{1g}}^{\ell\ell'} = g_{A_{1g}}^{\ell\ell} \delta_{\ell, \ell'} \quad (10)$$

Within the RPA^{73–75}, the spin susceptibility $\hat{\chi}^s(q)$ and the charge-orbital susceptibility $\hat{\chi}^c(q)$ are given in the 50×50 matrix representation as follows^{60–62,66},

$$\hat{\chi}^s(q) = [\hat{1} - \hat{\chi}^{(0)}(q)\hat{S}]^{-1}\hat{\chi}^{(0)}(q), \quad (11)$$

$$\hat{\chi}^c(q) = [\hat{1} + \hat{\chi}^{(0)}(q)\hat{C}]^{-1}\hat{\chi}^{(0)}(q) \quad (12)$$

with the noninteracting susceptibility

$$\chi_{\ell_1\ell_2,\ell_3\ell_4}^{(0)\alpha,\beta}(q) = -\frac{T}{N} \sum_k G_{\ell_3\ell_1}^{\beta\alpha}(k) G_{\ell_2\ell_4}^{\alpha\beta}(k+q), \quad (13)$$

where α, β ($=A, B$) represent two Fe sites, ℓ represents Fe 3d orbitals, $\hat{G}(k) = [(i\varepsilon_n + \mu)\hat{1} - \hat{H}_0(\mathbf{k})]^{-1}$ is the noninteracting Fe-3d electron Green's function in the 10×10 matrix representation, μ is the chemical potential, $\hat{H}_0(\mathbf{k})$ is the kinetic part of the Hamiltonian with the momentum \mathbf{k} in eq. (2), $k = (\mathbf{k}, i\varepsilon_n)$, $q = (\mathbf{q}, i\nu_m)$ and $\varepsilon_n = (2n+1)\pi T$ and $\nu_m = 2m\pi T$ are the fermionic and bosonic Matsubara frequencies, respectively. It is noted that when the largest eigenvalue $\lambda_{\text{spin}}(\lambda_{\text{c-o}})$ of $\hat{\chi}^{(0)}(q)\hat{S}$ ($-\hat{\chi}^{(0)}(q)\hat{C}$) reaches unity, the magnetic (charge-orbital) instability occurs.

In the RPA, generally, we need to collect all the ring- and ladder-type Feynman diagrams, where the bare vertices for the spin and charge-orbital susceptibilities \hat{S} and \hat{C} in eqs. (11) and (12) are given by⁶⁸

$$(\hat{S})_{\ell_1\ell_2,\ell_3\ell_4}^{\alpha,\beta} = (\hat{U}^s)_{\ell_1\ell_2,\ell_3\ell_4}^{\alpha,\beta}, \quad (14)$$

$$(\hat{C})_{\ell_1\ell_2,\ell_3\ell_4}^{\alpha,\beta} = (\hat{U}^c)_{\ell_1\ell_2,\ell_3\ell_4}^{\alpha,\beta} - 2\delta_{\alpha\beta} \sum_s g_s^{\ell_2\ell_1} g_s^{\ell_3\ell_4} D_s(i\nu_m), \quad (15)$$

where the $D_s(i\nu_m) = 2\omega_s/(\nu_m^2 + \omega_s^2)$ is the local phonon Green's function for the mode s and \hat{U}^s and \hat{U}^c are the bare vertices due to the Coulomb interaction given as follows,

$$\hat{U}^s (\hat{U}^c) = \begin{cases} U (U) & (\alpha = \beta, \ell_1 = \ell_2 = \ell_3 = \ell_4) \\ U' (-U' + 2J) & (\alpha = \beta, \ell_1 = \ell_3 \neq \ell_2 = \ell_4) \\ J (2U' - J) & (\alpha = \beta, \ell_1 = \ell_2 \neq \ell_3 = \ell_4) \\ J' (J') & (\alpha = \beta, \ell_1 = \ell_4 \neq \ell_2 = \ell_3) \\ 0 & (\text{otherwise}) \end{cases}. \quad (16)$$

In eqs. (14) and (15), we neglect the ladder terms for the phonon-mediated interaction. This is valid when the condition $\omega_s \ll E_F$ is satisfied, where E_F is the Fermi energy, because the ladder terms are proportional to the power of ω_s/E_F in the weak coupling regime under the condition $\omega_s \ll E_F$ ⁷⁶. The vertex corrections including the ladder terms, however, play significant roles in the intermediate and strong coupling regime even though $\omega_s \ll E_F$ ⁷⁷. The effect of the ladder terms will be discussed in Sec. III D.

The linearized Eliashberg equation is given by

$$\lambda_{\text{sc}} \Delta_{\ell\ell'}^{\alpha\beta}(k) = -\frac{T}{N} \sum_{k'} \sum_{\ell_1\ell_2,\ell_3\ell_4} \sum_{\alpha'\beta'} V_{\ell\ell_1,\ell_2\ell'}^{\alpha,\beta}(k-k') \times G_{\ell_3\ell_1}^{\alpha'\alpha}(-k') \Delta_{\ell_3\ell_4}^{\alpha'\beta'}(k') G_{\ell_4\ell_2}^{\beta'\beta}(k'), \quad (17)$$

where $\Delta_{\ell\ell'}^{\alpha\beta}(k)$ is the gap function and $V_{\ell_1\ell_2,\ell_3\ell_4}^{\alpha,\beta}(q)$ is the effective pairing interaction for the spin-singlet state. Within the RPA⁷³⁻⁷⁵, $V_{\ell_1\ell_2,\ell_3\ell_4}^{\alpha,\beta}(q)$ is given in the 50×50 matrix,

$$\hat{V}(q) = \frac{3}{2} \hat{S} \hat{\chi}^s(q) \hat{S} - \frac{1}{2} \hat{C} \hat{\chi}^c(q) \hat{C} + \frac{1}{2} (\hat{S} + \hat{C}). \quad (18)$$

The linearized Eliashberg equation (17) is solved to obtain the gap function $\Delta_{\ell\ell'}^{\alpha\beta}(k)$ with the eigenvalue λ_{sc} .

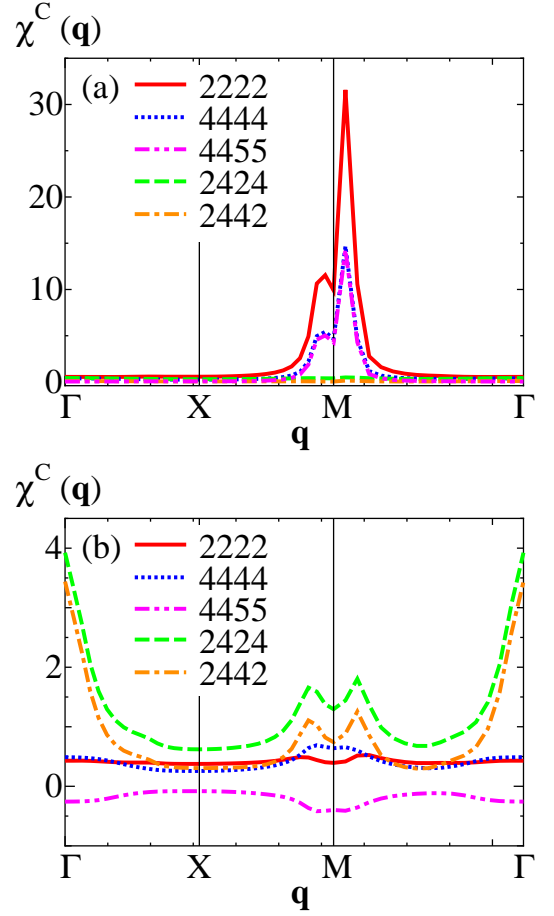


FIG. 3: (Color online) Several components of the charge-orbital susceptibility $\hat{\chi}^c(\mathbf{q}, 0)$ for $U' = 0$ and $2g^2/\omega_0 = 0.31$ (a) and those for $U' = 1.0$ and $2g^2/\omega_0 = 0.45$ at $J = J' = 0.1$ (b).

At $T = T_c$, the largest eigenvalue λ_{sc} becomes unity. In the present paper, we only focus on the case with $x = 0.1$, where the superconductivity is observed in the 1111 system². For simplicity, we set $T = 0.02\text{eV}$ and $\omega_{A_{1g}} = \omega_{B_{1g}} = \omega_{E_g^1} = \omega_{E_g^2} = \omega_0 = 0.02\text{eV}$ in the present study^{19,67,78}. As ref. 68, we assume $g_{E_g^1}^{15} = g_{E_g^1}^{34} = g_{E_g^2}^{14} = g_{E_g^2}^{35} = g_{B_{1g}}^{12} = 0$ and also set $g_{E_g^1}^{25} = g_{E_g^2}^{24} = g_{B_{1g}}^{44} = -g_{B_{1g}}^{55} = g_{A_{1g}}^{\ell\ell} = g$.

We use 32×32 \mathbf{k} point meshes and 512 Matsubara frequencies ($-511\pi T \leq \varepsilon_n \leq 511\pi T$) in the numerical calculations for eqs. (11)-(18), and perform the summation of the momentum and the frequency in eqs. (13) and (17) by using the fast Fourier transformation (FFT). Here and hereafter, we measure the energy in units of eV.

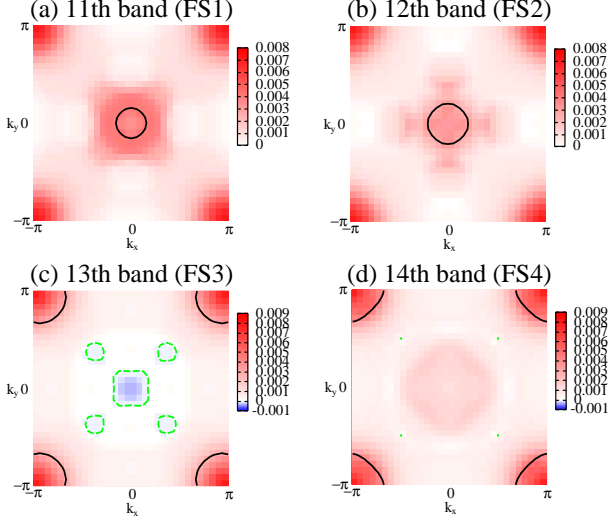


FIG. 4: (Color online) The diagonal components of the gap function $\hat{\Delta}(\mathbf{k}, i\pi T)$ in the band representation for $U' = 0$, $2g^2/\omega_0 = 0.31$ and $J = J' = 0.1$. (a), (b), (c) and (d) correspond to the 11th, 12th, 13th and 14th bands, respectively. The solid and dashed lines represent the FSs and the nodes of the gap function, respectively.

III. CALCULATED RESULTS

A. Charge-orbital susceptibility

As presented in eqs. (14) and (15), where we neglect the ladder terms, the spin susceptibility is not affected by the electron-phonon interaction and is the same as the results shown in our previous papers^{60–62,66}. Therefore, first, we focus on the effects of the electron-phonon interaction on the charge-orbital susceptibility. The effects of the ladder terms on the spin and charge-orbital susceptibilities will be discussed in Sec. III D.

The several components of the static charge-orbital susceptibility $\hat{\chi}^c(\mathbf{q}, 0)$ for $U' = 0$ and $2g^2/\omega_0 = 0.31$ and those for $U' = 1.0$ and $2g^2/\omega_0 = 0.45$ at $J = J' = 0.1$ are shown in Fig. 3 (a) and (b), respectively, where the parameters are chosen to satisfy the condition $\lambda_{sc} \sim 1$. It is found that for $U' = 0$ and $2g^2/\omega_0 = 0.31$, the diagonal components of $\hat{\chi}^c(\mathbf{q}, 0)$, especially $[\hat{\chi}^c(\mathbf{q}, 0)]_{22,22}^{A,A}$, are large and have sharp peaks around $\mathbf{q} \sim (\pi, \pi)$ which originate from the nesting between the hole FSs and the electron FSs (see Fig. 1), while the off-diagonal components are small. When $U' = 0$ and $2g^2/\omega_0 = 0.31$, $\lambda_{c-o} \sim 0.99$ and the charge susceptibility $\sum_{\ell, \ell', \alpha, \beta} [\hat{\chi}^c(\mathbf{q}, 0)]_{\ell\ell', \ell'\ell'}^{\alpha, \beta}$ becomes almost divergent, where the charge fluctuations dominate over the orbital fluctuations. We note that the charge-fluctuations are enhanced due to the effects of the A_{1g} phonon.

As shown in Fig. 3 (b), for $U' = 1.0$ and $2g^2/\omega_0 = 0.45$, the off-diagonal components of $\hat{\chi}^c(\mathbf{q}, 0)$, especially $[\hat{\chi}^c(\mathbf{q}, 0)]_{24,24}^{A,A}$ and $[\hat{\chi}^c(\mathbf{q}, 0)]_{24,42}^{A,A}$, are large and have

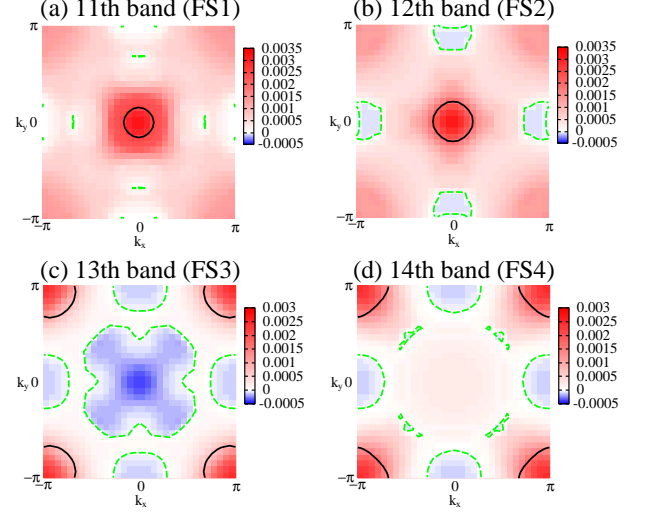


FIG. 5: (Color online) The diagonal components of the gap function $\hat{\Delta}(\mathbf{k}, i\pi T)$ in the band representation for $U' = 1.0$, $2g^2/\omega_0 = 0.45$ and $J = J' = 0.1$. (a), (b), (c) and (d) correspond to the 11th, 12th, 13th and 14th bands, respectively. The solid and dashed lines represent the FSs and the nodes of the gap function, respectively.

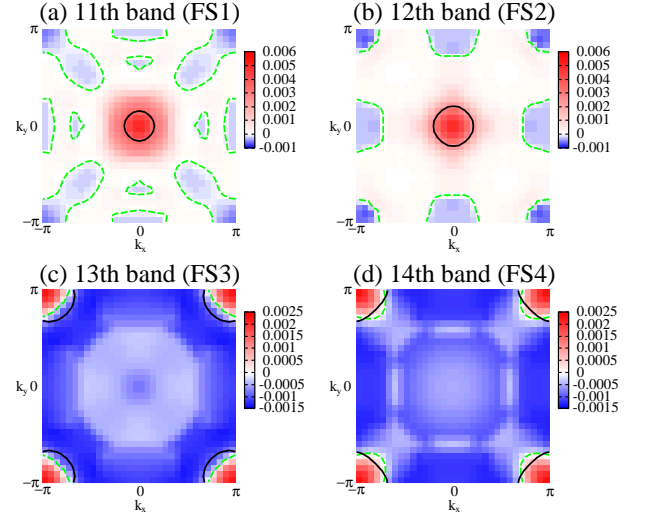


FIG. 6: (Color online) The diagonal components of the gap function $\hat{\Delta}(\mathbf{k}, i\pi T)$ in the band representation for $U' = 1.5$, $2g^2/\omega_0 = 0.34$ and $J = J' = 0.1$. (a), (b), (c) and (d) correspond to the 11th, 12th, 13th and 14th bands, respectively. The solid and dashed lines represent the FSs and the nodes of the gap function, respectively.

broad peaks around $\mathbf{q} = (0, 0)$ and $\mathbf{q} \sim (\pi, \pi)$, while the diagonal components are not so large in contrast to the case with $U' = 0$ and $2g^2/\omega_0 = 0.31$ (see Fig 3 (b)). We note that $[\hat{\chi}^c(\mathbf{q}, 0)]_{24,24}^{A,A}$ and $[\hat{\chi}^c(\mathbf{q}, 0)]_{24,42}^{A,A}$ represent the transverse orbital fluctuations. The peaks around $\mathbf{q} = (0, 0)$ and $\mathbf{q} \sim (\pi, \pi)$ originate from the scattering in the electron FSs and the nesting between the hole FSs

and the electron FSs, respectively. When $U' = 1.0$ and $2g^2/\omega_0 = 0.45$, $\lambda_{c-o} \sim 0.97$ and the off-diagonal components $[\hat{\chi}^c(\mathbf{q})]_{24,24}^{A,A}$ and $[\hat{\chi}^c(\mathbf{q})]_{24,42}^{A,A}$ are largely enhanced, while the charge susceptibility $\sum_{\ell,\ell',\alpha,\beta} [\hat{\chi}^c(\mathbf{q})]_{\ell\ell,\ell'\ell'}^{\alpha,\beta}$ is not enhanced because of the negative contributions of the orbital susceptibilities such as $[\hat{\chi}^c(\mathbf{q},0)]_{44,55}^{A,A}$ (see Fig. 3). Then, the orbital fluctuations dominate over the charge fluctuations in contrast to the case with $U' = 0$ and $2g^2/\omega_0 = 0.31$. We note that the off-diagonal components of the orbital susceptibilities $[\hat{\chi}^c(\mathbf{q},0)]_{24,24}^{A,A}$ and $[\hat{\chi}^c(\mathbf{q},0)]_{24,42}^{A,A}$ are enhanced due to the effects of the E_g phonon, while $[\hat{\chi}^c(\mathbf{q},0)]_{44,44}^{A,A}$ and $[\hat{\chi}^c(\mathbf{q},0)]_{44,55}^{A,A}$ are enhanced due to the effects of the B_{1g} phonon. In addition, the orbital fluctuations are enhanced also due to the effect of the inter orbital Coulomb interaction U' as shown in our previous paper⁶⁶.

B. Gap function

By solving the linearized Eliashberg equation, we obtain the gap function with the lowest Matsubara frequency in the orbital representation $\Delta_{\ell\ell'}^{\alpha\beta}(\mathbf{k}, i\pi T)$. Then performing the unitary transformation, we obtain the diagonal components of the gap function in the band representation $\hat{\Delta}(\mathbf{k}, i\pi T)$. Figs. 4 shows $\hat{\Delta}(\mathbf{k}, i\pi T)$ for $U' = 0$ and $2g^2/\omega_0 = 0.31$. It is found that the pairing symmetry is the s_{++} -wave state, where the gap function has no sign change on the whole FSs. In this regime, the s_{++} -wave superconductivity is mediated by the charge fluctuations which is enhanced due to the effects of the A_{1g} phonon as mentioned before (see Fig. 3 (a)).

Figs. 5 shows $\hat{\Delta}(\mathbf{k}, i\pi T)$ for $U' = 1.0$ and $2g^2/\omega_0 = 0.45$. It is found that the pairing symmetry is the s_{++} -wave state, where the gap function has no sign change on the whole FSs. In this regime, the s_{++} -wave superconductivity is mediated by the orbital fluctuations which is enhanced due to the cooperative effects of the B_{1g} , E_g phonons and the inter-orbital Coulomb interaction U' as mentioned before (see Fig. 3 (b)).

In contrast to the above two cases, for $U' = 1.5$ and $2g^2/\omega_0 = 0.34$, the gap function have nodes on the FS4 as shown in Fig. 6. Thus, the pairing state is the nodal s_{\pm} -wave state which originate from the coexistence of the orbital fluctuations with $\mathbf{q} = (0,0)$ and the spin fluctuations with $\mathbf{q} \sim (\pi, \pi)$ ^{60-62,66}. When we further increase the Coulomb interaction, the spin fluctuations dominate over the orbital fluctuations resulting in the s_{\pm} -wave state, where the sign of the gap function between the hole FSs and the electron FSs as shown in Fig. 7^{62,66}. Then, the nodal s_{\pm} -wave state is observed in the crossover region between the s_{\pm} -wave phase and the s_{++} -wave phase as shown in Fig. 7.

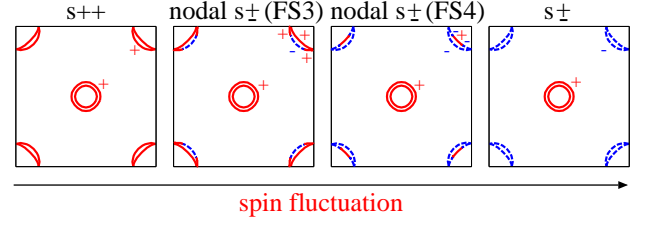


FIG. 7: (Color online) The schematic figure of the crossover between the s_{++} -wave and the nodal s_{\pm} -wave states and that between the nodal s_{\pm} -wave and the s_{\pm} -wave states. The solid and dashed lines represent the FSs on which the signs of the gap functions are positive and negative, respectively.

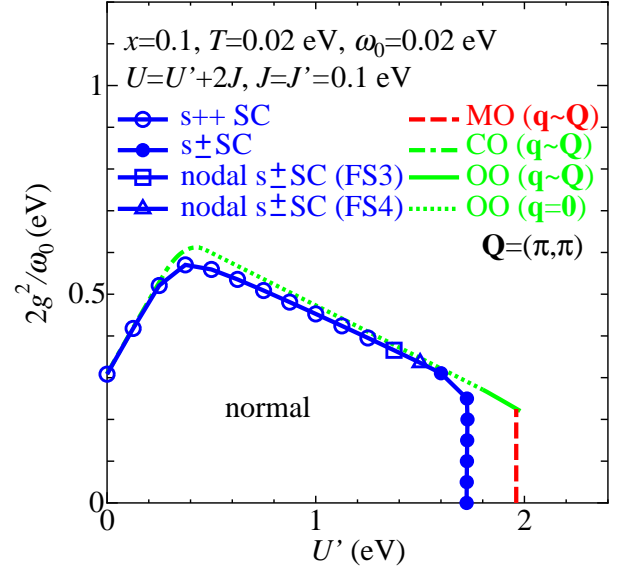


FIG. 8: (Color online) (a) The phase diagram on the U' - $2g^2/\omega_0$ plane for $J = J' = 0.1$ at $x = 0.1$, $T = 0.02$. The open and solid circles represent the s_{++} -wave and s_{\pm} -wave superconducting instabilities, respectively. The open triangles and squares represent the nodal s_{\pm} -wave superconducting instabilities whose nodes are on the FS3 and FS4, respectively. The dashed, solid, dotted, and dot-dashed lines show the magnetic order with $\mathbf{q} \sim (\pi, \pi)$, orbital order with $\mathbf{q} \sim (\pi, \pi)$, orbital order with $\mathbf{q} = (0, 0)$, and charge order with $\mathbf{q} \sim (\pi, \pi)$, respectively.

C. Phase diagram

The phase diagram on U' - $2g^2/\omega_0$ plane is shown in Fig. 8. It is found that the phase diagram includes the charge, orbital, and magnetic order and the superconductivity, where the charge-orbital, magnetic and superconducting instabilities are determined by the condition that λ_{c-o} , λ_{spin} and λ_{sc} reach unity as mentioned in Sec. II, respectively.

First, we focus on the ordered phase. As shown in Fig. 8, for $0 \leq U' < 0.44$, the charge order with $\mathbf{q} \sim (\pi, \pi)$

takes place at a certain critical value of $2g^2/\omega_0$. Since both the intra- and inter-orbital direct terms U and U' suppress the charge fluctuations, the critical values of $2g^2/\omega_0$ increase with increasing U' . For $0.44 < U' < 1.8$, the ferro orbital order with $\mathbf{q} = (0, 0)$ takes place, while the antiferro-like orbital order with $\mathbf{q} \sim (\pi, \pi)$ takes place for $1.8 < U' < 1.96$. Since the inter-orbital direct term U' enhances the orbital fluctuations⁶⁶, the critical values of $2g^2/\omega_0$ decrease with increasing U' . For $U' > 1.96$, the stripe-type AFM order with $\mathbf{q} \sim (\pi, \pi)$ takes place as presented in the previous papers^{60–62,66}.

Now, let us bring our attention to the superconductivity. It is found that the pairing symmetry is always s -wave and the gap structure sensitively depends on U' and $2g^2/\omega_0$. For $U' \leq 1.25$, the s_{++} -wave superconductivity is realized near the charge and orbital ordered phases. The superconductivity near the charge ordered phase is mediated by the charge fluctuations characterized by $[\hat{\chi}^c(\mathbf{q}, 0)]_{\ell\ell, \ell\ell}^{A,A}$, while that near the orbital ordered phase is mediated by the orbital fluctuations characterized by $[\hat{\chi}^c(\mathbf{q}, 0)]_{24, 24}^{A,A}$, $[\hat{\chi}^c(\mathbf{q}, 0)]_{24, 42}^{A,A}$, $[\hat{\chi}^c(\mathbf{q}, 0)]_{44, 44}^{A,A}$ and $[\hat{\chi}^c(\mathbf{q}, 0)]_{44, 55}^{A,A}$ (see Fig. 3). On the other hand, for $U' \geq 1.6$, the s_{\pm} -wave superconductivity is realized near the orbital and magnetic ordered phases, where the spin fluctuations are responsible for the superconductivity as presented in the previous papers^{60–62,66}. In addition, the nodal s_{\pm} -wave superconductivity is realized between the s_{++} -wave and s_{\pm} -wave superconducting phases.

This crossover behavior is naturally explained by the relative strength of the orbital fluctuations and the spin fluctuations. When the spin fluctuations are not so strong, the s_{++} -wave state is realized. With increasing U' , the spin fluctuations with $\mathbf{q} \sim (\pi, \pi)$ develop, especially $[\hat{\chi}^s(\mathbf{q}, 0)]_{22, 22}^{A,A}$. The gap function $\Delta_{22}^{AA}(\mathbf{k}, i\pi T)$ has sign change between the hole FSs and the electron FSs, where the amplitude of $\Delta_{22}^{AA}(\mathbf{k}, i\pi T)$ around the electron FSs is small. On the other hand, $\Delta_{44}^{AA}(\mathbf{k}, i\pi T)$ and $\Delta_{55}^{AA}(\mathbf{k}, i\pi T)$ have no sign change. As a result, the nodes appear on the FS3 which has mainly orbital 2 character. As the spin fluctuations with $\mathbf{q} \sim (\pi, \pi)$ further increase, the amplitude of $\Delta_{22}^{AA}(\mathbf{k}, i\pi T)$ around the electron FSs increase and the nodes appear on the FS4 and finally, for $U' \geq 1.6$, the fully-gapped s_{\pm} -wave state is realized. As shown in Fig. 7, the nodes firstly appear on the FS3 and the position of the nodes smoothly moves to FS4 as U' increases. Finally, the nodes on the FSs disappear and the s_{\pm} -wave state is realized.

We note that the critical value of $2g^2/\omega_0$ at which the orbital order takes place decrease with increasing U' as mentioned above, since U' enhances the orbital fluctuations⁶⁶. Thus, we stress that the orbital order and the orbital fluctuation-mediated superconductivity are driven by the cooperative effects of the Coulomb interaction and the electron-phonon interaction.

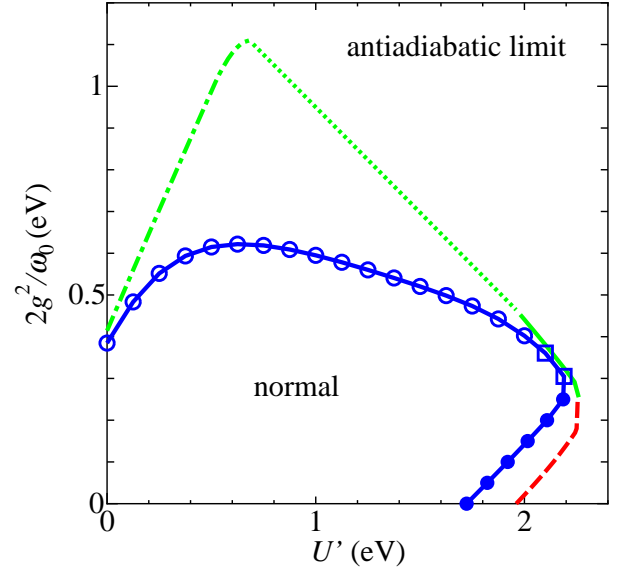


FIG. 9: (Color online) (a) The phase diagram on the U' - $2g^2/\omega_0$ plane for $J = J' = 0.1$ at $x = 0.1$, $T = 0.02$ in the antiadiabatic limit. It is noted that the legends are the same as Fig. 8

D. Antiadiabatic limit

Finally, we discuss the effects of the ladder type diagrams of the electron-phonon interaction which are neglected in eqs. (14) and (15). In general, it is difficult to include the effects of the ladder terms for the phonon-mediated interaction. Therefore, in this subsection, we study the effects of the ladder terms by taking the antiadiabatic limit ($\omega_s \rightarrow \infty$), where the phonon Green's function becomes $D_s(i\nu_m) \rightarrow 2/\omega_s$. The resulting bare vertices \hat{S} and \hat{C} are given by,

$$(\hat{S})_{\ell_1 \ell_2, \ell_3 \ell_4}^{\alpha\beta} = (\hat{U}^s)_{\ell_1 \ell_2, \ell_3 \ell_4}^{\alpha\beta} - 2\delta_{\alpha\beta} \sum_s g_s^{\ell_3 \ell_1} g_s^{\ell_2 \ell_4} / \omega_s, \quad (19)$$

$$(\hat{C})_{\ell_1 \ell_2, \ell_3 \ell_4}^{\alpha\beta} = (\hat{U}^c)_{\ell_1 \ell_2, \ell_3 \ell_4}^{\alpha\beta} - 2\delta_{\alpha\beta} \sum_s 2g_s^{\ell_2 \ell_1} g_s^{\ell_3 \ell_4} / \omega_s + 2\delta_{\alpha\beta} \sum_s g_s^{\ell_3 \ell_1} g_s^{\ell_2 \ell_4} / \omega_s. \quad (20)$$

Substituting eqs. (19) and (20) into eqs. (11), (12) and (18) instead of eqs. (14) and (15), we obtain the RPA results with including the ladder terms of the electron-phonon interaction. Although the antiadiabatic limit is not physically relevant, it is still a useful point of the reference for getting an overall understanding of the physics of the model. We note that, when we apply the antiadiabatic limit to the vertex \hat{C} given in eq. (15) where the ladder terms of the electron-phonon interaction are neglected, the phase boundaries for the charge, orbital and magnetic orders shown in Fig. 8 are unchanged although

the superconducting phase boundary is modified due to the retardation effect of the electron-phonon interactions as mentioned below.

The phase diagram on $U'-2g^2/\omega_0$ plane in the antiadiabatic limit is shown in Fig. 9. As shown in eq. (19), the spin fluctuation enhanced due to the 1st term of r.h.s. is suppressed by the 2nd term of r.h.s. corresponding to the contribution from the ladder terms of the electron-phonon interaction. Similarly, the charge-orbital fluctuation enhanced due to the 2nd term of r.h.s. in eq. (20) is suppressed by the 3rd term of r.h.s. corresponding to the contribution from the ladder terms. Therefore, the magnetic, charge and orbital instabilities are considered to be suppressed by the ladder terms of the electron-phonon interaction. In fact, as shown in Fig. 9, the critical values of $2g^2/\omega_0$ for the charge and orbital orders with including the ladder terms are larger than those without the ladder terms shown in Fig. 8. The critical value of U' for the magnetic order with including the ladder terms is also larger than that without the ladder terms (see Figs. 8 and 9).

Remarkably, the s_{++} -wave superconductivity is observed in a considerably wide parameter region as shown in Fig. 9. In the antiadiabatic limit, the bare vertex \hat{C} given in eq. (20) is independent of the frequency, and then, the effective pairing interaction $\hat{V}(q)$ due to the charge-orbital fluctuations becomes attractive for a wide frequency range. On the other hand, in the case with the frequency dependent vertex \hat{C} given in eq. (15), the effective pairing interaction $\hat{V}(q)$ due to the charge-orbital fluctuations becomes attractive only for the low frequency $|\nu_m| < \omega_0$. As the result, the s_{++} -wave superconductivity due to the charge-orbital fluctuations is observed in a relatively narrow region as shown in Fig. 8 for $T = \omega_0 = 0.02$, where $\hat{V}(q)$ is attractive only for ν_m with $m = 0$ as $\nu_1 = 2\pi T > \omega_0$. When the temperature is lowered below ω_0 , $\hat{V}(q)$ becomes attractive also for ν_m with $|m| \geq 1$, and then, it is expected that the s_{++} -wave superconductivity is observed in a wider parameter region also for the case with the frequency dependent vertex.

IV. SUMMARY AND DISCUSSION

In summary, we have investigated the two-dimensional 16-band d - p model coupled with A_{1g} , B_{1g} and E_g local phonons using the RPA and have obtained the phase diagram including the magnetic, charge and orbital ordered phases on the parameter plane of the Coulomb and electron-phonon interactions as follows: (1) For weak Coulomb interaction, the charge order with $\mathbf{q} \sim (\pi, \pi)$ takes place due to the effect of the electron-phonon interaction with A_{1g} mode. (2) For intermediate Coulomb interaction, the orbital order with $\mathbf{q} \sim (0, 0)$ takes place due to the cooperative effects of the Coulomb interaction and the electron-phonon interaction with B_{1g} and E_g modes. The orbital order with $\mathbf{q} \sim (\pi, \pi)$ also takes

place for relatively larger value of the Coulomb interaction. (3) For strong Coulomb interaction, the stripe-type antiferromagnetic order with $\mathbf{q} \sim (\pi, \pi)$ takes place due to the effect of the Coulomb interaction.

Using the effective pairing interaction obtained from the RPA, we have also solved the linearized Eliashberg equation to obtain the superconducting phase diagram including the three types of s -wave pairing as follows: (1) Near the charge ordered phase for weak Coulomb interaction, the s_{++} -wave pairing is mediated by the charge fluctuations. (2) Near the orbital ordered phase for intermediate Coulomb interaction, the s_{++} -wave pairing is mediated by the orbital fluctuations when the spin fluctuations are not so strong, while the nodal s_{\pm} -wave pairing is mediated by both of the orbital and spin fluctuations when the spin fluctuations are rather strong. (3) Near the magnetic ordered phase for strong Coulomb interaction, the s_{\pm} -wave pairing is mediated by the spin fluctuations.

Similar phase diagram including the magnetic and orbital ordered phases had recently been obtained by Kontani and Onari using the 5-band Hubbard-Holstein model⁶⁸. They had also discussed the superconductivity due to the magnetic and orbital fluctuations and have claimed that the s_{++} -wave superconductivity is realized near the orbital ordered phase, while the s_{\pm} -wave superconductivity is realized near the magnetic ordered phase, although the detailed superconducting phase diagram has not been obtained. In the present study, we have explicitly obtained the superconducting phase diagram and have found that not only the s_{++} -wave but also the nodal s_{\pm} -wave superconductivity is realized near the orbital ordered phase in contrast to the prediction in ref. 68. In addition, the charge order and the charge fluctuation-mediated s_{++} -wave superconductivity have been found to take place due to the effect of the A_{1g} local phonon which was not been considered in ref. 68. In early theoretical studies for the copper oxide superconductors, the effect of the Coulomb interaction between the d and p electrons U_{pd} was found to enhance the charge fluctuations which induce the s -wave superconductivity^{79,80}. We have also discussed the effect of U_{pd} on the present d - p model for the iron-based superconductors and have found that U_{pd} enhances the charge fluctuation-mediated s_{++} -wave superconductivity. The detailed results will be published in a subsequent paper.

It seems that both the s_{\pm} -wave and the s_{++} -wave states with full superconducting gaps are consistent with various experiments in the iron-based superconductors as mentioned in Sec. I, although the sign of the gap function has not been directly observed. However, the recent theoretical studies of the nonmagnetic impurity effects⁶⁵ revealed that the Anderson's theorem is violated for the s_{\pm} -wave superconductivity in contrast to the experimental results of very weak T_c suppression in Fe site substitution^{29,36} and neutron irradiation³². As the impurity potential due to the Fe-site substitution is considered to be diagonal and local in the orbital basis according to the first principle calculation⁸¹, it is expected that the

s_{++} -wave state is more robust against the nonmagnetic impurity than the s_{\pm} -wave state. In the recent ultrasonic measurements^{82,83}, a remarkable softening of the elastic constant is observed at low temperature down to T_c and is well accounted for by Jahn-Teller modes coupled with strong orbital fluctuations⁸³. In addition, the weak T -dependence of $1/T_1T$ ^{43,84} above T_c in the electron-doped compounds is considered to indicate the weak spin fluctuations. Thus, the s_{++} -wave state due to the orbital fluctuations seems to be responsible for the fully gapped superconductivity in the iron-based superconductors.

In $\text{BaFe}_2(\text{As}_{1-x}\text{P}_x)_2$, the recent field-angle resolved specific heat⁸⁵ and the ARPES measurements⁸⁶ suggest that the superconducting gap function has vertical line nodes along the k_z -axis on the electron FSs. This nodal superconductivity seems to correspond to the nodal s_{\pm} -wave state obtained in the present study. In the previous works^{50,56,87}, the similar nodal s_{\pm} -wave states have been obtained in the crossover region between the s_{\pm} -wave phase and the d -wave phase when the different modes of the spin fluctuations coexist. This is a striking contrast to the case with the present study where the nodal s_{\pm} -wave state is realized in the crossover region between the s_{++} -wave phase and the s_{\pm} -wave phase when the strong orbital and spin fluctuations coexist. If the fully gapped superconductivity widely observed in the iron-based superconductors is the s_{++} -wave state, it is natural to consider that the nodal superconductivity observed in $\text{BaFe}_2(\text{As}_{1-x}\text{P}_x)_2$ is the nodal s_{\pm} -wave state obtained in the present study.

In the present and previous papers⁶⁶, we have shown that the electron-phonon interaction plays important roles for the iron-based superconductors in cooperation with the Coulomb interaction. Actually, the Raman spectroscopies indicate the large electron-phonon interaction⁶⁷. The large value of the Grüneisen

parameter⁸⁸ and the drastic softening of the elastic constant^{82,83} observed in $\text{BaFe}_{2-x}\text{Co}_x\text{As}_2$ also indicate the large electron-lattice coupling. Remarkably, the recent ultrasonic measurements revealed that the softening of the elastic constant C_{44} is much larger than $(C_{11} - C_{12})/2$ and continues down to T_c ⁸³, where the temperature dependence of the elastic constant is well accounted for by Jahn-Teller modes which couple with the orbital fluctuation between d_{yz} and d_{zx} orbitals: $[\chi^c(q)]_{44,44}^{\alpha,\beta} - [\chi^c(q)]_{44,55}^{\alpha,\beta}$. Since this type of the orbital fluctuation is enhanced due to the electron-phonon interaction with B_{1g} mode, we may expect that the effects of the B_{1g} phonon is most dominant for the elastic softening and the superconductivity. In fact, the first principle calculation¹⁹ and the Raman spectroscopies^{67,78} suggest that the frequency of the B_{1g} phonon is lower than the A_{1g} and E_g phonons, although the same frequencies are assumed in the present study for simplicity. Therefore, we need further investigation of the electron-phonon interaction with including the more realistic effects such as the mode dependence of the phonon frequencies and the coupling constants and the phonon dispersions which have not been considered in this paper.

Acknowledgments

The authors thank M. Yoshizawa, M. Sato, H. Kon-tani, S. Onari, T. Nomura, H. Ikeda, K. Kuroki and Y. Yanase for useful comments and discussions. This work was partially supported by the Grant-in-Aid for Scientific Research from the Ministry of Education, Culture, Sports, Science and Technology. The authors Y. Yanagi and Y. Yamakawa are supported by the Grant-in-Aid for JSPS Fellows.

- ¹ Y. Kamihara, H. Hiramatsu, M. Hirano, H. Y. R. Kawamura, T. Kamiya, and H. Hosono, *J. Am. Chem. Soc.* **128**, 10012 (2006).
- ² Y. Kamihara, T. Watanabe, M. Hirano, and H. Hosono, *J. Am. Chem. Soc.* **130**, 3296 (2008).
- ³ G. F. Chen, Z. Li, D. Wu, G. Li, W. Z. Hu, J. Dong, P. Zheng, J. L. Luo, and N. L. Wang, *Phys. Rev. Lett.* **100**, 247002 (2008).
- ⁴ Z. A. Ren, J. Yang, W. Lu, W. Yi, X. L. D. G. C. Che, L. L. Sun, and Z. X. Zhao, *Mater. Res. Innovations* **12**, 105 (2008).
- ⁵ Z. A. Ren, J. Yang, W. Lu, W. Yi, X. L. Shen, G. C. C. Z. C. Li, X. L. Dong, L. L. Sun, F. Zhou, and Z. X. Zhao, *Europhys. Lett.* **82**, 57002 (2008).
- ⁶ X. H. Chen, T. Wu, G. Wu, R. H. Liu, H. Chen, and D. F. Fang, *Nature* **453**, 761 (2008).
- ⁷ Z. A. Ren, W. Lu, J. Yang, W. Yi, X. L. Shen, G. C. C. Z. C. Li, X. L. Dong, L. L. Sun, F. Zhou, and Z. X. Zhao, *Chin. Phys. Lett.* **25**, 2215 (2008).
- ⁸ M. Rotter, M. Tegel, D. Johrendt, I. Schellenberg, W. Her-

- mes, and R. Pottgen, *Phys. Rev. B* **78**, 020503(R) (2008).
- ⁹ M. Rotter, M. Tegel, and D. Johrendt, *Phys. Rev. Lett.* **101**, 107006 (2008).
- ¹⁰ X. C. Wang, Q. Q. Liu, Y. X. Lv, W. B. Gao, L. X. Yang, R. C. Yu, F. Y. Li, and C. Q. Jin, *Solid State Commun.* **148**, 538 (2008).
- ¹¹ M. J. Pitcher, D. R. Parker, P. Adamson, S. J. C. Herkelrath, A. T. Boothroyd, R. M. Ibberson, M. Brunelli, and S. J. Clarke, *Chem. Commun.* p. 5918 (2008).
- ¹² J. H. Tapp, Z. Tang, B. Lv, K. Sasmal, B. Lorenz, P. C. W. Chu, and A. M. Guloy, *Phys. Rev. B* **78**, 060505(R) (2008).
- ¹³ F.-C. Hsu, J.-Y. Luo, K.-W. Yeh, T.-K. Chen, T.-W. Huang, P. M. Wu, Y.-C. Lee, Y.-L. Huang, Y.-Y. Chu, D.-C. Yan, et al., *Proc. Natl. Acad. Sci. U.S.A.* **105**, 14262 (2008).
- ¹⁴ K.-W. Yeh, T.-W. Huang, Y.-L. Huang, T.-K. Chen, F.-C. Hsu, P. Wu, Y.-C. Lee, Y.-Y. Chu, C.-L. Chen, J.-Y. Luo, et al., *Europhys. Lett.* **84**, 37002 (2008).
- ¹⁵ S. Lebegue, *Phys. Rev. B* **75**, 035110 (2007).
- ¹⁶ D. J. Singh and M. H. Du, *Phys. Rev. Lett.* **100**, 237003

- (2008).
- 17 K. Haule, J. H. Shim, and G. Kotliar, *Phys. Rev. Lett.* **100**, 226402 (2008).
 - 18 G. Xu, W. Ming, Y. Yao, X. Dai, S.-C. Zhang, and Z. Fang, *Europhys. Lett.* **82**, 67002 (2008).
 - 19 L. Boeri, O. V. Dolgov, and A. A. Golubov, *Phys. Rev. Lett.* **101**, 026403 (2008).
 - 20 I. A. Nekrasov, Z. V. Pchelkina, and M. V. Sadovskii, *JETP Lett.* **88**, 144 (2008).
 - 21 I. A. Nekrasov, Z. V. Pchelkina, and M. V. Sadovskii, *JETP Lett.* **88**, 543 (2008).
 - 22 A. Subedi, L. Zhang, D. J. Singh, and M. H. Du, *Phys. Rev. B* **78**, 134514 (2008).
 - 23 F. Ma, W. Ji, J. Hu, Z.-Y. Lu, and T. Xiang, *Phys. Rev. Lett.* **102**, 177003 (2009).
 - 24 H. Ding, P. Richard, K. Nakayama, T. Sugawara, T. Arakane, Y. Sekiba, A. Takayama, S. Souma, T. Sato, T. Takahashi, et al., *Europhys. Lett.* **83**, 47001 (2008).
 - 25 D. H. Lu, M. Yi, S.-K. Mo, A. S. Erickson, J. Analytis, J.-H. Chu, D. J. Singh, Z. Hussain, T. H. Geballe, I. R. Fisher, et al., *Nature* **455**, 81 (2008).
 - 26 M. Yi, D. H. Lu, J. G. Analytis, J.-H. Chu, S.-K. Mo, R.-H. He, X. J. Zhou, G. F. Chen, J. L. Luo, N. L. Wang, et al., *Phys. Rev. B* **80**, 024515 (2009).
 - 27 C. de la Cruz, Q. Huang, J. W. Lynn, J. Li, W. R. II, J. L. Zarestky, H. A. Mook, G. F. Chen, J. L. Luo, N. L. Wang, et al., *Nature* **453**, 899 (2008).
 - 28 K. Matano, Z. A. Ren, X. L. Dong, L. L. Sun, Z. X. Zhao, and G. Q. Zheng, *Europhys. Lett.* **83**, 57001 (2008).
 - 29 A. Kawabata, S. C. Lee, T. Moyoshi, Y. Kobayashi, and M. Sato, *J. Phys. Soc. Jpn.* **77**, 103704 (2008).
 - 30 K. Hashimoto, T. Shibauchi, T. Kato, K. Ikada, R. Okazaki, H. Shishido, M. Ishikado, H. Kito, H. E. A. Iyo, S. Shamoto, et al., *Phys. Rev. Lett.* **102**, 017002 (2009).
 - 31 G. Mu, X. Zhu, L. Fang, L. Shan, C. Ren, and H. H. Wen, *Chin. Phys. Lett.* **25**, 2221 (2008).
 - 32 A. E. Karkin, J. Werner, G. Behr, and B. N. Goshchitskii, arXiv:0904.1634.
 - 33 Y. Nakai, K. Ishida, Y. Kamihara, M. Hirano, and H. Hosono, *J. Phys. Soc. Jpn.* **77**, 073701 (2008).
 - 34 Y. Kobayashi, A. Kawabata, S. C. Lee, and M. S. T. Moyoshi, *J. Phys. Soc. Jpn.* **78**, 073704 (2009).
 - 35 Q. Huang, Y. Qiu, W. Bao, M. A. Green, J. W. Lynn, Y. C. Gasparovic, T. Wu, G. Wu, and X. H. Chen, *Phys. Rev. Lett.* **101**, 257003 (2008).
 - 36 A. S. Sefat, R. Jin, M. A. McGuire, B. C. Sales, D. J. Singh, and D. Mandrus, *Phys. Rev. Lett.* **101**, 117004 (2008).
 - 37 M. Yashima, H. Nishimura, H. Mukuda, Y. Kitaoka, K. Miyazawa, P. M. Shirage, K. Kihou, H. Kito, H. Eisaki, and A. Iyo, *J. Phys. Soc. Jpn.* **78**, 103702 (2009).
 - 38 K. Hashimoto, T. Shibauchi, S. Kasahara, K. Ikada, T. K. S. Tonegawa, R. Okazaki, C. J. van der Beek, M. Konczykowski, H. Takeya, K. Hirata, et al., *Phys. Rev. Lett.* **102**, 207001 (2009).
 - 39 H. Liu, W. Zhang, L. Zhao, X. Jia, J. Meng, G. Liu, X. Dong, G. F. Chen, N. L. W. J. L. Luo, W. Lu, et al., *Phys. Rev. B* **78**, 184514 (2008).
 - 40 T. Kondo, A. F. Santander-Syro, O. Copie, C. Liu, M. E. Tillman, E. D. Mun, J. Schmalian, S. L. Bud'ko, M. A. Tanatar, P. C. Canfield, et al., *Phys. Rev. Lett.* **101**, 147003 (2008).
 - 41 S. Jiang, H. Xing, G. Xuan, C. Wang, C. F. Z. Ren, J. D. Z. Xu, and G. Cao, *J. Phys.: Condens. Matter* **21**, 382203 (2009).
 - 42 K. Hashimoto, M. Yamashita, S. Kasahara, Y. Senshu, N. Nakata, S. Tonegawa, K. Ikada, A. Serafin, A. Carrington, T. Terashima, et al., arXiv:0907.4399.
 - 43 Y. Nakai, T. Iye, S. Kitagawa, K. Ishida, S. Kasahara, T. Shibauchi, Y. Matsuda, and T. Terashima, *Phys. Rev. B* **81**, 020503(R) (2010).
 - 44 M. H. Fang, H. M. Pham, B. Qian, T. J. Liu, E. K. Vehstedt, Y. Liu, L. Spinu, and Z. Q. Mao, *Phys. Rev. B* **78**, 224503 (2008).
 - 45 W. Bao, Y. Qiu, Q. Huang, M. A. Green, P. Zajdel, M. R. Fitzsimmons, M. Zhernenkov, S. Chang, M. Fang, B. Qian, et al., *Phys. Rev. Lett.* **102**, 247001 (2009).
 - 46 J. K. Dong, T. Y. Guan, S. Y. Zhou, X. Qiu, L. Ding, C. Zhang, U. Patel, Z. L. Xiao, and S. Y. Li, *Phys. Rev. B* **80**, 024518 (2009).
 - 47 I. I. Mazin, D. J. Singh, M. D. Johannes, and M. H. Du, *Phys. Rev. Lett.* **101**, 057003 (2008).
 - 48 K. Kuroki, S. Onari, R. Arita, H. Usui, Y. Tanaka, H. Kontani, and H. Aoki, *Phys. Rev. Lett.* **101**, 087004 (2008).
 - 49 K. Kuroki, S. Onari, R. Arita, H. Usui, Y. Tanaka, H. Kontani, and H. Aoki, *New J. Phys.* **11**, 025017 (2009).
 - 50 K. Kuroki, H. Usui, S. Onari, R. Arita, and H. Aoki, *Phys. Rev. B* **79**, 224511 (2009).
 - 51 T. Nomura, *J. Phys. Soc. Jpn.* **78**, 0347160 (2009).
 - 52 H. Ikeda, *J. Phys. Soc. Jpn.* **77**, 123707 (2008).
 - 53 H. Ikeda, R. Arita, and J. Kuneš, *Phys. Rev. B* **81**, 054502 (2010).
 - 54 F. Wang, H. Zhai, Y. Ran, A. Vishwanath, and D. H. Lee, *Phys. Rev. Lett.* **102**, 047005 (2009).
 - 55 S. Graser, T. A. Maier, P. J. Hirschfeld, and D. J. Scalapino, *New J. Phys.* **11**, 025016 (2009).
 - 56 T. A. Maier, S. Graser, D. J. Scalapino, and P. J. Hirschfeld, *Phys. Rev. B* **79**, 224510 (2009).
 - 57 Z. J. Yao, J. X. Li, and Z. D. Wang, *New J. Phys.* **11**, 025009 (2009).
 - 58 T. D. Stanescu, V. Galitski, and S. DasSarma, *Phys. Rev. B* **78**, 195114 (2008).
 - 59 V. Cvetkovic and Z. Teseanovic, *Europhys. Lett.* **85**, 37002 (2009).
 - 60 Y. Yanagi, Y. Yamakawa, and Y. Ōno, *J. Phys. Soc. Jpn. Suppl. C* **77**, 149 (2008).
 - 61 Y. Yanagi, Y. Yamakawa, and Y. Ōno, *J. Phys. Soc. Jpn.* **77**, 123701 (2008).
 - 62 Y. Yanagi, Y. Yamakawa, and Y. Ōno, to be published in *Physica C*.
 - 63 K. Seo, B. A. Bernevig, and J. Hu, *Phys. Rev. Lett.* **101**, 206404 (2008).
 - 64 K. Sano and Y. Ōno, *J. Phys. Soc. Jpn.* **78**, 124706 (2009).
 - 65 S. Onari and H. Kontani, *Phys. Rev. Lett.* **103**, 177001 (2009).
 - 66 Y. Yanagi, Y. Yamakawa, and Y. Ōno, *Phys. Rev. B* **81**, 054518 (2010).
 - 67 M. Rahlenbeck, G. L. Sun, D. L. Sun, C. T. Lin, B. Keimer, and C. Ulrich, *Phys. Rev. B* **80**, 064509 (2009).
 - 68 H. Kontani and S. Onari, *Phys. Rev. Lett.* **104**, 157001 (2010).
 - 69 V. Vildosola, L. Pourovskii, R. Arita, S. Biermann, and A. Georges, *Phys. Rev. B* **78**, 064518 (2008).
 - 70 K. Nakamura, R. Arita, and M. Imada, *J. Phys. Soc. Jpn.* **77**, 093711 (2008).
 - 71 T. Miyake, K. Nakamura, R. Arita, and M. Imada, *J. Phys. Soc. Jpn.* **79**, 0447105 (2010).
 - 72 Y. Yamakawa, Y. Yanagi, and Y. Ōno, in preparation.
 - 73 T. Takimoto, T. Hotta, and K. Ueda, *Phys. Rev. B* **69**,

- 104504 (2004).
- ⁷⁴ M. Mochizuki, Y. Yanase, and M. Ogata, Phys. Rev. Lett. **94**, 147005 (2005).
- ⁷⁵ K. Yada and H. Kontani, J. Phys. Soc. Jpn. **74**, 2161 (2005).
- ⁷⁶ A. B. Migdal, Sov. Phys. JETP **7**, 996 (1958).
- ⁷⁷ J. P. Hague and N. d'Ambrumenil, J. Low. Temp. Phys. **151**, 1149 (2008).
- ⁷⁸ S. C. Zhao, D. Hou, Y. Wu, T. L. Xia, A. M. Zhang, G. F. Chen, J. L. Luo, N. L. Wang, J. H. Wei, Z. Y. Lu, et al., Supercond. Sci. Technol. **22**, 015017 (2009).
- ⁷⁹ P. B. Littlewood, C. M. Varma, and E. Abrahams, Phys. Rev. Lett. **63**, 2602 (1989).
- ⁸⁰ D. S. Hirashima, Y. Ōno, T. Matsuura, and Y. Kuroda, J. Phys. Soc. Jpn. **61**, 649 (1992).
- ⁸¹ A. F. Kemper, C. Cao, P. J. Hirschfeld, and H.-P. Cheng, Phys. Rev. B **80**, 104511 (2009).
- ⁸² R. M. Fernandes, L. H. VanBebber, S. Bhattacharya, P. Chandra, V. Keppens, D. Mandrus, M. A. McGuire, B. C. Sales, A. S. Sefat, and J. Schmalian, arXiv:0911.3084.
- ⁸³ M. Yoshizawa, private communication.
- ⁸⁴ T. Nakano, N. Fujiwara, K. Tatsumi, H. Okada, H. Takahashi, Y. Kamihara, M. Hirano, and H. Hosono, Phys. Rev. B **81**, 100510(R) (2010).
- ⁸⁵ Y. Matsuda, private communication.
- ⁸⁶ T. Shimojima, private communication.
- ⁸⁷ T. Kariyado and M. Ogata, J. Phys. Soc. Jpn. **79**, 037703 (2010).
- ⁸⁸ S. L. Bud'ko, N. Ni, S. Nandi, G. M. Schmiedeshoff, and P. C. Canfield, Phys. Rev. B **79**, 054525 (2009).